

The $^{13}\text{C}(\alpha, n)$ reaction and its role as a neutron source for the s process

M. Heil,^{1,*} R. Detwiler,^{2,†} R. E. Azuma,^{2,3} A. Couture,^{2,‡} J. Daly,^{2,§} J. Görres,² F. Käppeler,¹ R. Reifarth,^{1,||} P. Tischhauser,^{2,¶} C. Ugalde,^{2,**} and M. Wiescher²

¹*Forschungszentrum Karlsruhe, Institut für Kernphysik, Postfach 3640, D-76021 Karlsruhe, Germany*

²*University of Notre Dame, Department of Physics, Notre Dame, Indiana 46556, USA*

³*University of Toronto, Toronto, Ontario, M5S 1A7, Canada*

(Received 17 April 2008; published 12 August 2008)

The $^{13}\text{C}(\alpha, n)^{16}\text{O}$ reaction constitutes the dominant neutron source for the main s process, which operates at a thermal energy of $kT = 8$ keV. Since the cross section at stellar energies is very small, the reaction rate cannot be directly determined and has to be extrapolated from cross section results obtained at higher energies. To remove various discrepancies in the normalization of previous data sets and to subsequently improve the reliability of the extrapolation, we performed measurements of the $^{13}\text{C}(\alpha, n)^{16}\text{O}$ reaction in the energy range $E_{\text{c.m.}} = 320\text{--}700$ keV. In addition, the double differential scattering cross section $^{13}\text{C}(\alpha, \alpha)^{13}\text{C}$ was measured in the energy range $E_{\text{lab}} = 2.6\text{--}6.2$ MeV for 28 angles. These data were used to constrain possible contributions from background resonances for a reliable extrapolation with the multichannel R -matrix code SAMMY. As a result, the uncertainties were significantly reduced, and a reaction rate of $(4.6 \pm 1.0) \times 10^{-14}$ cm³/moles at $kT = 8$ keV ($T = 0.1 \times 10^9$ K) was determined.

DOI: [10.1103/PhysRevC.78.025803](https://doi.org/10.1103/PhysRevC.78.025803)

PACS number(s): 25.55.Hp, 25.40.Lw, 25.55.Ci, 26.20.-f

I. INTRODUCTION

Current stellar models as well as stellar spectroscopy strongly support the $^{13}\text{C}(\alpha, n)^{16}\text{O}$ reaction as the dominant neutron source for the main component of the s process in thermally pulsing, low-mass, asymptotic giant branch (TP-AGB) stars [1]. The energy generation in such stars occurs in the H and He burning shells surrounding the inert C/O core. The H and He burning shells are separated by a thin He-rich intershell region. During H burning, the intershell becomes more and more enriched in He until the He concentration and the temperature are high enough for igniting He burning at the bottom of the intershell. This He shell flash spreads out through the full intershell. Because of the heat generated during the He burning, the intershell becomes convective, and the star expands and cools in the outer layers with the consequence that H burning is temporarily terminated. The He shell flash ends after about 200 yr when most of the He has been consumed; the star contracts again and H burning is reactivated. These alternating H and He burning phases are repeated up to 40 times.

The main s process is assumed to take place during the phase prior to the He flash when hydrogen is mixed from the convective envelope into the He intershell after the preceding thermal pulse. This mixing mechanism is not yet fully understood and is presently the subject of several studies (see, e.g., Refs. [2–5]). The protons are captured by ^{12}C , and ^{13}C is produced by the reaction sequence $^{12}\text{C}(p, \gamma)^{13}\text{N}(\beta^- \nu)^{13}\text{C}$. This leads to the formation of the so-called ^{13}C pocket, a thin layer enriched in ^{13}C . After some time, the temperature reaches values of $\approx 0.1 \times 10^9$ K, high enough to generate neutrons by the $^{13}\text{C}(\alpha, n)^{16}\text{O}$ reaction, which triggers the s process.

Because the abundances of the Fe-group nuclei in the ^{13}C pocket, which act as seed for the s process, are limited, the neutron/seed ratio is large. This translates into a very efficient production of heavy s -process nuclei over a long period of time. Later, during the convective He shell flash, the freshly synthesized s -process material of the ^{13}C pocket is mixed and diluted over the He intershell. A second neutron exposure occurs when the temperature at the bottom of the convective shell flash reaches values of $(250\text{--}300) \times 10^6$ K liberating neutrons by the $^{22}\text{Ne}(\alpha, n)^{25}\text{Mg}$ reaction. This second neutron exposure contributes only about 5% to the total exposure. It is, therefore, not sufficient to produce s isotopes on a grand scale, but it is strong enough to alter the abundance ratios of the isotopes in s -process branchings. After the He flash, part of the processed material is mixed into the convective envelope and transported to the surface of the star.

The neutron density during the s process depends crucially on three parameters that still carry some uncertainties: the rate of the $^{13}\text{C}(\alpha, n)^{16}\text{O}$ reaction, the amount of protons mixed into the He-rich intershell, which determines the abundance of ^{13}C in the pocket, and finally the destruction of ^{13}C via $^{13}\text{C}(p, \gamma)^{14}\text{N}$ reactions. This study will focus on the first problem by seeking to reduce the uncertainty associated with the $^{13}\text{C}(\alpha, n)^{16}\text{O}$ cross section.

*Present address: GSI Darmstadt, Planckstr. 1, D-64291 Darmstadt, Germany; M.Heil@gsi.de

†Present address: University of Florida, Department of Nuclear and Radiological Engineering, P.O. Box 118300, Gainesville, FL 32611-8300, USA.

‡Present address: Los Alamos National Laboratory, Los Alamos, NM 87545, USA.

§Present address: Center for Naval Analysis, 4825 Mark Center Dr., Alexandria, VA 22311-1850, USA.

||Present address: GSI Darmstadt, Planckstr. 1, D-64291 Darmstadt, Germany.

¶Present address: Microsoft Corp., Redmond, WA 98052, USA.

**Present address: Department of Physics, University of North Carolina, CB3255, Chapel Hill, NC 27599, USA.

The temperature during the *s* process in the ^{13}C pocket of 90×10^6 K (corresponding to a thermal energy of $kT = 8$ keV) corresponds to a Gamow window around 190 keV (140–230 keV) for the (α, n) reaction on ^{13}C . Since this energy is far below the Coulomb barrier, the reaction cross section is extremely small and not accessible to direct measurements. For this reason, its value has to be determined by extrapolation of the cross sections measured at higher energies. The extrapolation is complicated by the unknown influence of a broad subthreshold state with $J^\pi = 1/2^+$ at $E_x = 6.356$ MeV ($E_\alpha^{\text{lab}} = -3$ keV), and by two subthreshold resonances with $J^\pi = 1/2^-$ at $E_x = 5.939$ MeV ($E_\alpha^{\text{lab}} = -547$ keV) and $J^\pi = 3/2^+$ at $E_x = 5.869$ MeV ($E_\alpha^{\text{lab}} = -641$ keV).

The main impact on the extrapolation is expected from the $1/2^+$ state at 6.356 MeV, which is situated close to the threshold. This was suggested by a microscopic cluster model analysis of the $^{13}\text{C}(\alpha, n)$ and $^{13}\text{C}(\alpha, \alpha)$ reactions [6] and experimentally underlined by a recent indirect asymptotic normalization coefficient (ANC) analysis of this particular level [7], which was based on an α transfer measurement. While this analysis suggested an appreciable strength for this resonance, other α transfer data led to an ambiguous interpretation for the strength of this particular state [8,9] in the $^{13}\text{C}+\alpha$ reaction channels. In addition, recent attempts to measure the $^{13}\text{C}(\alpha, n)^{16}\text{O}$ cross section toward very low energies could not provide unambiguous information on the energy dependence of the *S* factor in the Gamow window [10]. All extrapolations of previous low-energy cross section data [11–14] are characterized by large uncertainties and correspondingly large variations of the predicted stellar reaction rates.

In this paper, we present the results of new $^{13}\text{C}+\alpha$ capture and scattering experiments, which have been performed to improve the extrapolation of the $^{13}\text{C}(\alpha, n)^{16}\text{O}$ cross section. In a first step, the absolute $^{13}\text{C}(\alpha, n)$ cross section was measured in the energy range $E_{\text{lab}} = 420$ –900 keV to resolve the discrepancies between previous data sets [10,15–18]. This experiment and the results are described in Sec. II. Second, the double differential scattering cross section $^{13}\text{C}(\alpha, \alpha)^{13}\text{C}$ was measured for 29 angles and 275 energy steps over the energy range $E_{\text{lab}} = 2.5$ –6.2 MeV to constrain possible low-energy contributions from background resonances. The experimental setup and the results of this second measurement are outlined in Sec. III. Finally, an extensive multichannel *R*-matrix analysis was carried out, which considered all possible reaction channels over a wide energy range. This analysis, which was performed with the computer code SAMMY, is described in Sec. IV. The final results and implications for the stellar reaction rate of $^{13}\text{C}(\alpha, n)^{16}\text{O}$ are discussed in Sec. V. A complete and rather detailed account of this work can be found in Ref. [19].

II. LOW-ENERGY MEASUREMENT OF THE $^{13}\text{C}(\alpha, n)^{16}\text{O}$ REACTION

The $^{13}\text{C}(\alpha, n)^{16}\text{O}$ experiment was performed at the Karlsruhe 3.7 MV Van de Graaff accelerator with α beams of typically 50 μA . Neutrons were detected with the Karlsruhe 4π BaF₂ calorimeter [20,21], which consists of 42 BaF₂

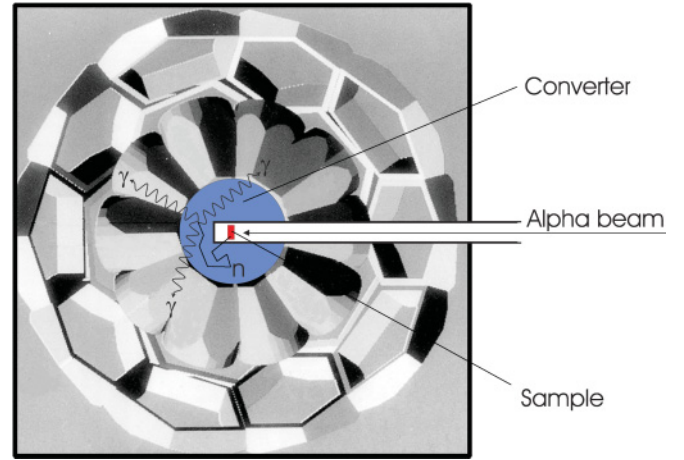


FIG. 1. (Color online) Modified 4π BaF₂ calorimeter. Neutrons from (α, n) reactions in the ^{13}C target are moderated and captured in the converter surrounding the target.

crystals forming a closed shell with an inner diameter of 20 cm and a thickness of 15 cm. Only 41 crystals were mounted during the experiment to leave space for the beam pipe. The detector was originally designed for high-precision (n, γ) measurements, but it was transformed into an efficient neutron detector by mounting a n/γ converter inside the BaF₂ shell. For the present (α, n) measurement, the beamline was extended into the center of the detector, where the α beam impinges on the ^{13}C target. This target was surrounded by a spherical cadmium-loaded paraffin shell with an outer diameter of 20 cm and a cadmium content of 3% (see Fig. 1). Neutrons from (α, n) reactions in the ^{13}C target were moderated in the paraffin and then captured in the Cd admixture, mostly by ^{113}Cd , which has the highest thermal (n, γ) cross section of all Cd isotopes. Finally, the capture γ -ray cascades were detected with an efficiency of about 95% by the 4π BaF₂ calorimeter.

Because of the high γ efficiency of the calorimeter, the γ cascades from $^{113}\text{Cd}(n, \gamma)^{114}\text{Cd}$ reactions yield a total energy signal of 9043 keV corresponding to the binding energy of the captured neutrons. These signals appear well separated from low-energy γ backgrounds. In addition, the multiplicity of the capture cascades could be used for further background reduction. These features are illustrated in Fig. 2.

The following description is focused on those aspects crucial to the accuracy of the measurement, i.e., detector efficiency, target performance, and beam energy definition (for further information, see Ref. [19]).

A. Efficiency for neutron detection

The neutron efficiency of the modified 4π BaF₂ calorimeter was measured using the $^{51}\text{V}(p, n)^{51}\text{Cr}$ reaction in a setup identical to the ^{13}C experiment. For this purpose, the ^{13}C targets in the center of the detector were replaced by ^{51}V targets and bombarded in separate runs with proton beams of 1700, 2500, and 3500 keV, yielding neutrons with energies of 135, 935, and 1935 keV, respectively. The total number of neutrons per run could be precisely defined by the produced ^{51}Cr activity, which was measured via the characteristic 320 keV γ line in the decay of ^{51}Cr . Counting this activity

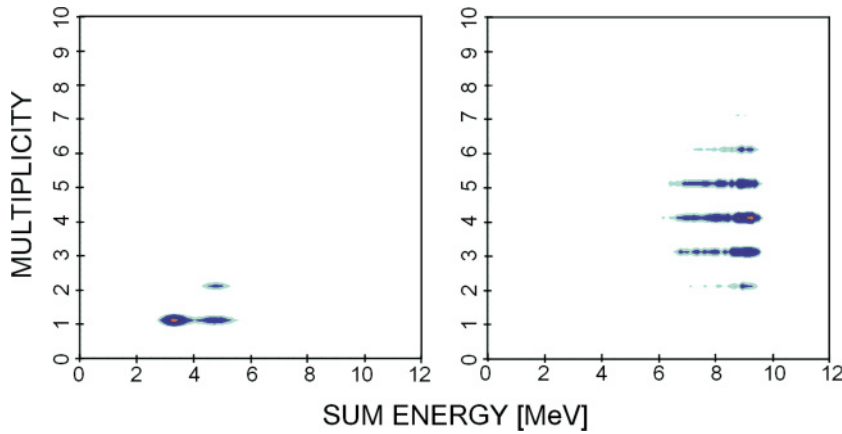


FIG. 2. (Color online) Response of the 4π BaF_2 calorimeter to background events (left) and to neutron captures on the Cd admixture of the paraffin converter surrounding the ^{13}C target (right).

under almost background-free conditions with a well-calibrated HPGe detector yielded the neutron efficiency at the above energies with an accuracy of 1.8%.

Since the Q value of the $^{13}\text{C}(\alpha, n)^{16}\text{O}$ reaction is 2215.61 keV, the neutrons are emitted with initial energies of up to 3 MeV. Therefore, the measured detection efficiencies had to be extrapolated to higher energies by detailed Monte Carlo simulations with the GEANT toolkit [22]. For these simulations, the experimental setup was modeled in great detail, as shown in Fig. 1, including the measured properties of the individual BaF_2 modules, i.e., their resolution in γ -ray energy. The neutron efficiency calculated in this way is plotted in Fig. 3, which compares the simulated efficiency curve with the measured values. The discrepancies at the lowest data points were caused by the $^{51}\text{V}(p, \gamma)^{52}\text{Cr}$ reactions. Because of the high Q value of 10.504 MeV, signals from this reaction could not be distinguished from the γ -ray cascades of true neutron captures in the Cd converter. The largest correction of 8% had to be applied at the lowest neutron energy of 135 keV. With this correction, the simulated and measured neutron efficiencies are in excellent agreement within the uncertainties of the experimental values.

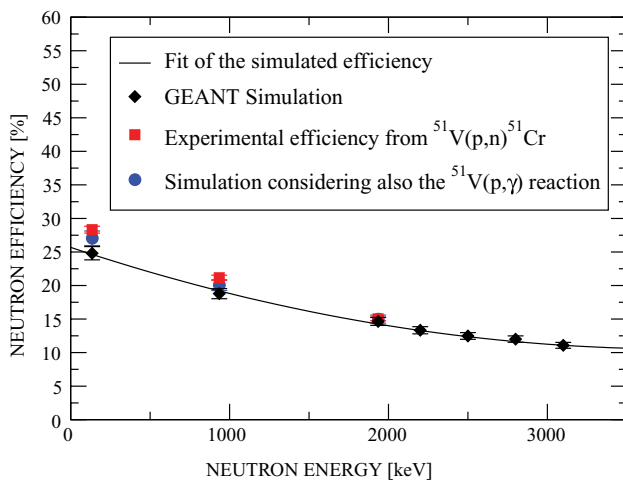


FIG. 3. (Color online) Measured and simulated neutron efficiency of the setup. The measured points below 1 MeV had to be corrected for contributions from (p, γ) reactions on ^{51}V .

The parametrized efficiency (in %) as a function of neutron energy (in units of keV),

$$\epsilon(E_n) = (1.03 \times 10^{-6})E_n^2 - 0.0079E_n + 25.684, \quad (1)$$

has been used in further data analysis.

B. Target preparation and performance

Thin ^{13}C layers were produced by ACF-Metals¹ by electron gun evaporation of 99% isotopically enriched material. The target backings consisted of water-cooled copper sheets, which were covered by $5\text{ }\mu\text{m}$ thick gold layers to minimize backgrounds from impurities in the copper. The thickness of the ^{13}C layer of $22\text{ }\mu\text{g cm}^{-2}$ was measured during evaporation with an oscillating quartz (see also Ref. [23]). In addition, the thickness and profile of the ^{13}C layers were measured before and after each experimental run using the narrow resonance at $E_p = 448.5\text{ keV}$ in the $^{13}\text{C}(p, \gamma)^{14}\text{N}$ reaction ($\Gamma = 0.37\text{ keV}$). Figure 4 shows an example of the measured thick target yield vs proton energy.

During the experiment, the target could be rotated by 180° . In this way, regular background measurements were performed

¹Arizona Carbon Foil Co., Inc., 2239 East Kleindale Rd., Tucson, AZ, USA.

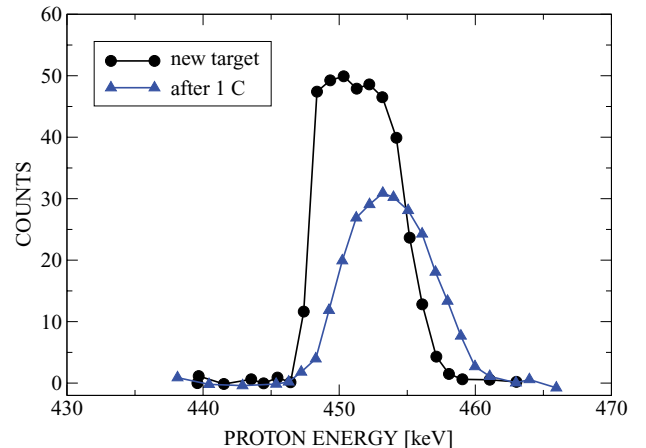


FIG. 4. (Color online) Reaction yield of the $^{13}\text{C}(p, \gamma)$ resonance at 448.5 keV for a fresh target and after an integrated charge of 1 C.

TABLE I. Measured and simulated neutron efficiencies of the experimental setup.

Neutron energy (keV)	Neutrons produced ($\times 10^7$)	Neutrons detected ($\times 10^7$)	$\epsilon_n(\%)$	
			Measured	Simulated
135	4.05	1.1463	28.3 ± 0.5	27.0
935	1.42	0.3001	21.2 ± 0.4	20.0
1935	3.32	0.4998	15.0 ± 0.3	15.0

by irradiating the gold-plated rear side of the target. A cold trap in the last part of the beamline was used to reduce carbon buildup on the surface of the ^{13}C layer. The target was electrically insulated and served as a Faraday cup for beam current measurements. Secondary electrons were suppressed by a voltage of -200 V that was applied to the cold trap and the beamline in front of the Faraday cup.

C. Beam energy calibration

The energy of the α beam was calibrated via the $^7\text{Li}(\alpha, \gamma)^{11}\text{B}$ reaction [24]. This reaction is particularly well suited since the three narrow resonances listed in Table II cover exactly the investigated energy range. The calibrations were performed with LiF targets, and the 8665 keV γ rays from the (α, γ) reaction were measured with a NaI detector.

D. Data analysis

The yield $Y(E_\alpha)$ per mC can be described by

$$Y(E_\alpha) = np\epsilon(E_\alpha) \int_{E_\alpha - \Delta}^{E_\alpha} \frac{\sigma(E)}{T(E)} dE, \quad (2)$$

where n denotes the number of α particles, p the enrichment of the ^{13}C samples, ϵ the neutron efficiency, E_α the beam energy, T the stopping power, and Δ the energy loss caused by the sample thickness. Since the measured yield corresponds to the integral of the energy-dependent term σ/T , the cross section cannot be extracted directly. Instead, an iterative approach was used, where the cross section was substituted by the S factor defined by

$$\sigma(E) = \frac{1}{E} \exp(-2\pi\eta) S(E), \quad (3)$$

TABLE II. Resonances of the $^7\text{Li}(\alpha, \gamma)^{11}\text{B}$ reaction used for the energy calibration of the α beam.

Energy E_{res} (keV)	Width Γ (eV)	J^π	Strength $\omega\gamma$ (eV)
402 ± 3	4.37 ± 0.02	$5/2^-$	0.0088
814 ± 2	1.8 ± 1.5	$7/2^+$	0.31
953 ± 2	4000	$5/2^+$	1.72

TABLE III. Experimental S factors.

E_{lab} (keV)	$E_{\text{c.m.}}$ (keV)	Yield (mC^{-1})	S factor (10^6 MeV b)	Uncertainties (%)	
				Stat.	Sys.
416	318	0.97	1.17	92	11
437	334	2.4	1.07	45	30
439	336	2.0	0.80	42	40
449	343	3.4	1.14	23	23
493	377	21.4	1.11	4.3	17
536	403	46.1	1.05	3.4	31
568	435	119	0.92	1.8	11
642	491	1034	1.11	1.8	6.4
695	531	3525	1.19	0.9	9.3
747	571	12169	1.48	0.5	9.0
800	612	32567	1.55	0.8	4.7
849	649	76240	1.70	0.2	5.0
899	687	175813	2.00	0.1	5.0

η being the Sommerfeld parameter. The S factor was expanded in terms of a Taylor series

$$S(E) = S(0) \left(1 + \frac{\dot{S}(0)}{S(0)} E + \frac{1}{2} \frac{\ddot{S}(0)}{S(0)} E^2 + \dots \right). \quad (4)$$

The term $S(0)$ and the derivatives with respect to energy, $\dot{S}(0)$ and $\ddot{S}(0)$, were iteratively obtained by fits of the experimental yields. The resulting S factor is valid for the respective beam energy. The stopping power of α particles and protons in carbon were adopted from Ref. [25]. It should be mentioned that the stopping power can vary with carbon type. But since the sample thickness was determined via the $^{13}\text{C}(p, \gamma)$ reaction, the results depend only on the more reliable ratio of stopping powers for protons and α particles in the same carbon layer.

E. Results and uncertainties

With this approach, the $^{13}\text{C}(\alpha, n)^{16}\text{O}$ reaction yield was measured in 13 energy steps between $E_{\text{lab}} = 416$ and 900 keV, which corresponds to target thicknesses between 8.7 and 5.4 keV. The reaction yields and the corresponding S factors are listed in Table III with their statistical and systematic uncertainties.

At lower energies, the systematic uncertainties are dominated by changes in sample thickness. These long runs, which were necessary for collecting sufficient statistics, suffered from carbon buildup and from diffusion of carbon into the gold layer. These effects are illustrated in Fig. 4 by the comparison of the reaction yields of the $^{13}\text{C}(p, \gamma)$ resonance at 448.5 keV for a fresh target and after an integrated charge of 1 C. The reduced width of the irradiated target corresponds to a loss of ^{13}C from sputtering effects, whereas the resonance shift toward higher beam energies is caused by an energy loss due to the buildup of a surface layer. Moreover, the lower plateau value indicates a change in target composition, presumably because of mixing of ^{13}C with ^{12}C in the growing surface layer and because of diffusion of ^{13}C into the Au coating of the backing.

Because of these significant target effects, it is mandatory to characterize the ^{13}C layers by additional measurements.

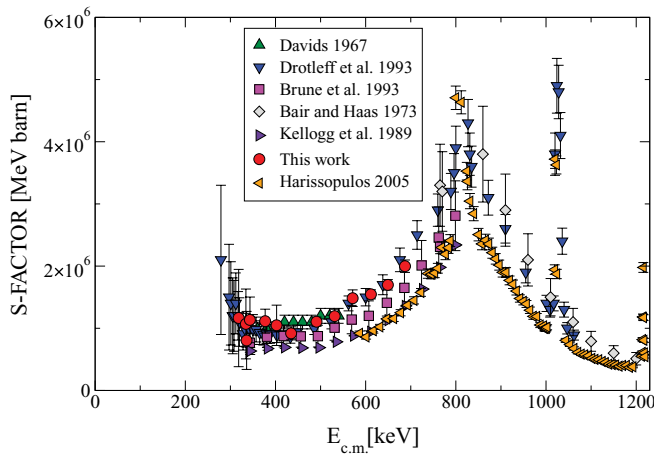


FIG. 5. (Color online) Present S factors compared with previous data.

This was achieved independent of particle type and energy by regular runs at 800 keV α energy. In this way, the effective thickness of the ^{13}C layers was determined before and after each measurement, and half the difference was adopted as a conservative estimate of the related uncertainty. Therefore, the systematic uncertainties depend also on the time between successive target characterization runs.

Because of the rapidly falling cross section, the uncertainties at lower energies are clearly dominated by limitations in counting statistics. At higher energies, where systematic uncertainties dominate, overall uncertainties could be reduced to the level of 5%.

F. Comparison with previous data

The present S -factor results are shown in Fig. 5 in comparison with data from previous experiments. Although there is good agreement with the S -factor data of Davids [15], Bair and Haas [16], and Drotleff *et al.* [10], the measurement by Kellogg *et al.* [17] reports systematically smaller S -factor values. A reevaluation of these data by Brune *et al.* [18] adopting a different normalization resulted in much better agreement with the present values, but the S factors still seem to be systematically smaller by $\approx 15\%$ than the trend of the other data sets.

More recently, a measurement of the $^{13}\text{C}(\alpha, n)^{16}\text{O}$ cross section by Harissopulos *et al.* [26], which covers a wide energy range using enriched ^{13}C targets with a thickness of ≈ 35 keV at 1 MeV beam energy, claims an overall uncertainty of 4% for the mean cross section data. At low energies, the cross section data seem to support the results of Kellogg *et al.* [17], which are slightly lower than the present values. The largest uncertainty in the results of Ref. [26] is related to the neutron efficiency, which was determined mainly by Monte Carlo simulations of the detector system. These simulations were checked against the low mean neutron energy of 2.3 MeV of a ^{252}Cf source, while the neutrons from the $^{13}\text{C}(\alpha, n)$ reaction are released with much higher energies. Therefore, systematic deviations cannot be excluded for the data of Harissopulos *et al.* [26], in contrast to the present work,

where the neutron efficiency was experimentally verified over a range of well-defined energies.

Accordingly, it appears that the inherent systematic uncertainty of the present data is more accurately controlled. Therefore, and in view of the good agreement with the results of Refs. [10,15,16], the further analysis of the reaction data is based on our values.

III. MEASUREMENT OF $^{13}\text{C}(\alpha, \alpha)^{13}\text{C}$ ELASTIC SCATTERING

The double differential scattering cross section of α particles on ^{13}C was measured at the Nuclear Structure Laboratory of the University of Notre Dame over a wide energy range and with high angular resolution. A first campaign was carried out at the 10 MV Pelletron tandem accelerator with a beam of doubly charged α particles. The beam was focused onto ^{13}C targets 8 mm in diameter, which were mounted in the center of a large scattering chamber. The position of the beam on the target was defined by two pairs of slits in front of the chamber. A cold trap at the entrance of the chamber served to minimize ^{12}C buildup on the sample as shown in the schematic sketch of the setup in Fig. 6.

The chamber contained 29 silicon detectors at laboratory angles of $43.9^\circ, 48.9^\circ, 54.0^\circ, 58.9^\circ, 63.9^\circ, 68.9^\circ, 74.0^\circ, 75.8^\circ, 79.0^\circ, 80.8^\circ, 84.0^\circ, 85.8^\circ, 89.0^\circ, 90.8^\circ, 94.0^\circ, 95.8^\circ, 99.0^\circ, 100.8^\circ, 103.9^\circ, 105.8^\circ, 110.8^\circ, 115.8^\circ, 120.8^\circ, 125.8^\circ, 130.8^\circ, 140.8^\circ, 150.8^\circ, 160.8^\circ$, and 165.8° . These detectors were mounted on both sides of the beam axis as indicated in Fig. 6 with an overlapping angular range of about 90° . Collimators 8.9 mm in diameter in front of the detectors were used to define the solid angle with respect to the ^{13}C targets in the center. Only for the most forward detector at an angle of 43.9° , the diameter of the collimator had to be reduced to 5.5 mm. The distance from the center of the target to the collimators was 587 mm.

The targets with a ^{13}C enrichment of 99.9% were between 9.6 and 12.1 g cm $^{-2}$ in thickness. Up to three targets were mounted on a sample ladder at an angle of 45° relative to the beam axis. The ladder carried also an empty position and a collimator 4 mm in diameter for the exact positioning of the beam. The beam current measured with a Faraday cup at the exit of the chamber was corrected for the effective charge state after passing through the carbon targets [28]. Secondary electrons were suppressed by means of a ring at a potential of -200 V.

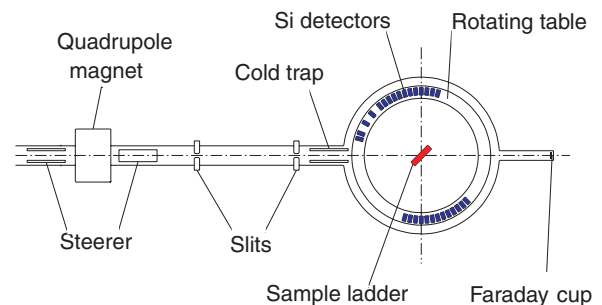


FIG. 6. (Color online) Setup for the measurement of the double differential cross section for α scattering on ^{13}C (not to scale).

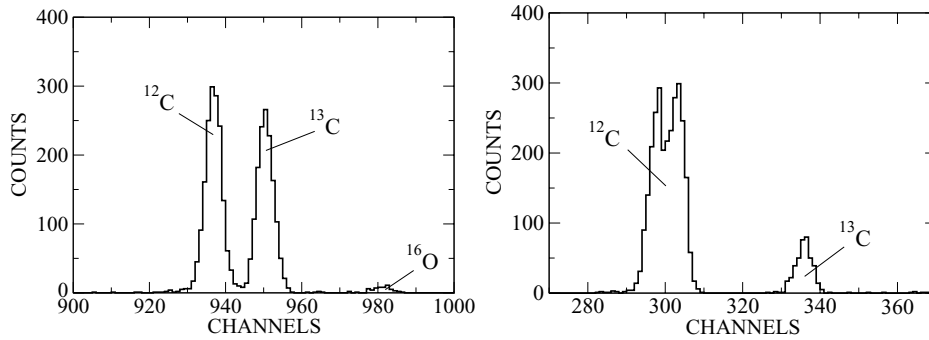


FIG. 7. Scattering spectra measured at 6.2 MeV laboratory energy for detectors at 44° (left) and 165° (right) with respect to the beam axis. The ^{12}C peaks are enhanced because the spectra were taken at the energy of a resonance in the $^{12}\text{C}(\alpha, \alpha)$ cross section. This example was chosen to illustrate that the effect of carbon buildup on the target surface was well under control. Normally, the spectra are dominated by scattering on ^{13}C .

The silicon detectors were mounted on a rotating table, and the exact angles of the detectors were determined with a telescope to a precision of better than 0.05° . However, the effective uncertainty of the scattering angles was 0.1° because of the 1.5 mm uncertainty of the beam spot position. In addition, the forward angles were checked via Mott scattering of a ^{12}C beam on a ^{12}C target at an energy of 6.02 MeV, since the interference pattern of the scattering of like particles provides a sensitive test for angular shifts. The beam energy was calibrated using a narrow resonance in the elastic scattering cross section of ^{12}C at 5247.3 keV.

Figure 7 shows typical spectra measured at 44° and 165°. The peaks from elastic scattering on ^{12}C and ^{13}C were clearly separated for most of the angles.

During this first campaign, the scattering cross section was measured between 2.9 and 6.2 MeV. In a second campaign, the differential cross section for $^{13}\text{C}(\alpha, \alpha)$ elastic scattering was measured in the energy range between 2.5 and 3.5 MeV at the 3.5 MV KN Van de Graaff accelerator of the University of Notre Dame. For this experiment, a smaller scattering chamber was used with eight Si detectors mounted at laboratory angles of 45.0°, 65.0°, 85.0°, 105.0°, 105.0°, 125.0°, 145.0°, and 165.0° with respect to the beam direction.

In this case, the collimators in front of the detectors were chosen from 0.89 to 3.68 mm in diameter, adapted to the count rates at different angles. With decreasing energy it became more and more difficult to separate the two peaks from elastic scattering on ^{12}C and ^{13}C , especially at forward angles. This effect became the limiting factor for the accessible energy range of the experiment.

While the energy of the α beam from the tandem accelerator was calibrated via the well-known resonance in the $^{12}\text{C}(\alpha, \alpha)^{12}\text{C}$ scattering cross section at 5247.3 keV ($\Gamma = 0.5$ keV), the energy calibration at the 3.5 MV Van de Graaff accelerator was performed using the resonance in the $^6\text{Li}(\alpha, \alpha)^6\text{Li}$ reaction at 2428.8 ± 0.5 keV ($\Gamma = 6$ keV) [29]. This calibration was further verified using the resonance of the $^{14}\text{N}(\alpha, \gamma)^{18}\text{O}$ reaction at 1529 ± 2 keV ($\Gamma = 1.2$ keV) [30].

A. Data analysis and results

The data from the two campaigns were analyzed following identical procedures. The number of α particles passing the ^{13}C target was measured with the Faraday cup at the exit of the scattering chamber. The effective charge state I was calculated following the formalism of reference [28].

The differential cross section can be calculated as

$$\frac{d\sigma}{d\Omega} = \frac{ZM_{13\text{C}}}{f_1 f_2 N_\alpha \frac{\rho h}{\sin\phi} N_A \Omega}, \quad (5)$$

where Z is the number of counts in the ^{13}C peak, $M_{13\text{C}}$ the mass of the ^{13}C target, N_α the number of α particles passing the target, and N_A Avogadro's number. The term $\rho h / \sin\phi$ stands for the areal density, and ϕ is the angle of the target relative to the beam axis. The factors f_1 and f_2 represent the corrections for the dead time of the data acquisition system and for the charge state distribution, respectively.

The data were also corrected for ^{12}C buildup to avoid a systematic shift in the energy of the α beam. The ^{12}C buildup, which was monitored by repeated measurements at an energy of 6.2 MeV, was found to increase linearly with the accumulated charge. However, even for the targets with highest exposure, this correction for energy loss in the ^{12}C layer was only 0.8 keV and could, therefore, be neglected.

The total uncertainties of the data points are dominated by the 10% systematic uncertainty of the ^{13}C thickness. Other systematic uncertainties, i.e., from sputtering losses of the ^{13}C target, could be eliminated by the regular reference measurements at 6.2 MeV. The duration of the measurements was chosen such that the statistical uncertainty of the detector with the lowest count rate was always $\leq 10\%$.

Figure 8 shows the measured excitation curve at a laboratory angle of 165° compared with previous data [31,32]. In both previous experiments, the excitation curve was measured at four angles, but only the data at 165° are tabulated.

IV. R-MATRIX ANALYSIS

As discussed in Sec. I, the measured $^{13}\text{C}(\alpha, n)^{16}\text{O}$ cross section has to be extrapolated to the lower energy range corresponding to the temperatures in the ^{13}C pocket. Under stellar conditions, reactions occur between 140 and 230 keV, much below the experimentally accessible energy region. The method of choice for this extrapolation is the R -matrix approach [33]. However, the quality of this approach depends on the complete consideration of the contributions from nearby resonances, of the interference effects from the tails of broad high-energy states, and of possible subthreshold levels.

As pointed out in previous theoretical work, the contributions of the broad $J^\pi = 1/2^+$ level at an excitation energy of 6.356 MeV, just 3 keV below the reaction threshold, are of importance in this context [6]. Two additional subthreshold levels with $J^\pi = 1/2^-$ and $3/2^+$ at 5.939 and 5.869 MeV

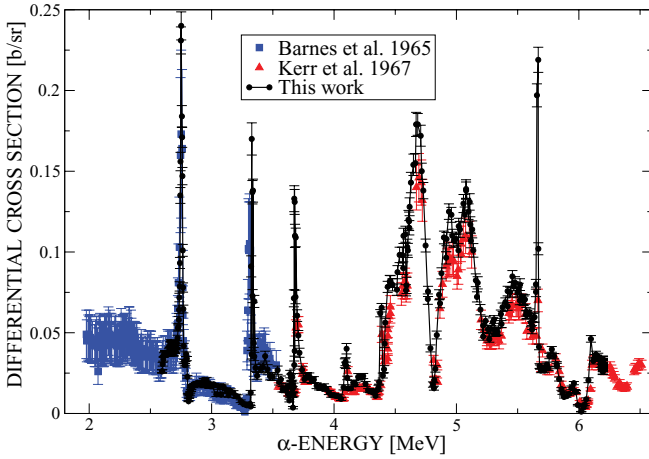


FIG. 8. (Color online) Differential cross section for elastic scattering of α particles on ^{13}C in the laboratory system at an angle of 165° compared with previous data [31,32]. The error bars correspond to the statistical uncertainties only.

excitation may have also a significant impact on the cross section at low energies. In particular, the $3/2^+$ state may interfere directly with the broad $3/2^+$ resonance state at 7.248 MeV. In addition, contributions from the tails of broad resonances at higher energy have to be considered as well.

In a compound system as complex as ^{17}O above the α threshold at 6.359 MeV, the R matrix can only be treated reliably by considering all subthreshold states and resonances over a wide energy range in order to take the interference patterns for all possible reaction channels into account. This implies that all available data for all reaction channels leading to the ^{17}O compound system should be included in the analysis. Two recent attempts [7,34] limited the R -matrix approach to the $^{13}\text{C}(\alpha, n)^{16}\text{O}$ reaction channel in a limited energy range near the α threshold while adopting information about the considered resonance levels from the literature [35]. Such an approach may suffer from systematic uncertainties, since the tabulated values have been obtained under different assumptions concerning the choice of reaction model parameters.

The impact of other reaction channels such as $^{16}\text{O}(n, n)^{16}\text{O}$, $^{16}\text{O}(n, \alpha)^{13}\text{C}$, and $^{13}\text{C}(\alpha, \alpha)^{13}\text{C}$, which had been included in an earlier multichannel R -matrix analysis of the $^{13}\text{C}(\alpha, n)^{16}\text{O}$ reaction [14], has led, for example, to a pronounced increase in the low-energy S -factor data.

The large amount of new experimental low-energy α capture and scattering data necessitates a new, comprehensive R -matrix study. To increase the reliability of the extrapolation toward low energies, a multichannel R -matrix analysis was carried out using the code SAMMY [36] including all open reaction channels for the $^{13}\text{C}+\alpha$ and the $^{16}\text{O}+n$ system. In this approach, we have fitted simultaneously all available experimental data on $^{13}\text{C}+\alpha$ and $^{16}\text{O}+n$ reaction and scattering channels including the full set of bound states in ^{17}O and unbound resonance states up to 10 MeV excitation energy. Since the entrance channel configurations $^{16}\text{O}+n$ and $^{13}\text{C}+\alpha$ cannot be fitted simultaneously with the R -matrix code SAMMY, both configurations were treated separately, and the

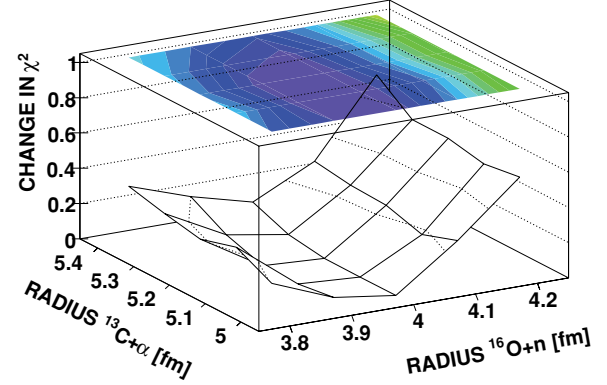


FIG. 9. (Color online) Variation of the radii for the $^{13}\text{C}+\alpha$ and the $^{16}\text{O}+n$ channels.

resonance parameters were varied until the sum of the χ^2 values of all individual runs was minimized.

Since the $^{13}\text{C}(\alpha, n)^{16}\text{O}$ cross section at low energies is most important for the purpose of this analysis, the χ^2 values of the high- and low-energy data sets were weighted by factors 10 [16,37] and 20 (Refs. [10,15,18] and this work), respectively. This is justified, because the small number of data points at low energies would otherwise have no significant impact, and the overall χ^2 value would be dominated by the numerous data for the elastic scattering cross section and the total cross section of ^{16}O .

To check the results for the effect of the channel radius, fits were performed for various combinations of channel radii (Fig. 9). The best solutions were obtained for a radius of 5.2 fm for the $^{13}\text{C}+\alpha$ channel and 4.0 fm for the $^{16}\text{O}+n$ channel.

In the following sections, we describe the various reaction and scattering data sets and the normalization procedures necessary for generating a consistent set of cross section data, and discuss the quality of the resulting fits.

A. Total neutron cross section of ^{16}O

Various data sets for the total neutron cross section of ^{16}O are available in the literature. For an R -matrix analysis, data sets covering a large energy range are especially valuable. The four selected sets listed in Table IV have superior energy resolution and cover the neutron energy range from 0.8 keV up to 10 MeV. The data of Cierjacks *et al.* [38] had to be renormalized by a factor of 0.95 to be consistent with the other sets.

Figure 10 shows the excellent agreement between the 17 118 data points of the references in Table IV and the R -matrix fit. The respective χ^2 values of the individual data sets are given in the table.

B. Double differential cross section $^{16}\text{O}(n, n)^{16}\text{O}$

The data sets used for this reaction channel are listed in Table V. The data of Lane *et al.* [42] cover the neutron energy range between 0.1 and 1.9 MeV corresponding to the excitation energies of α bound states in ^{17}O . The data show a small energy shift compared to the results of Shouky *et al.* [43], which was

TABLE IV. Data sets for the total neutron cross section of ^{16}O .

Authors	Facility	Energy range (MeV)	Data points	Ref.	χ^2
Cierjacks <i>et al.</i> (1968)	FZK Cyclotron	0.67–3.2	2737	[38]	4.6
Fowler <i>et al.</i> (1973)	ORNL VdG	0.59–4.3	538	[39]	6.2
Cierjacks <i>et al.</i> (1980)	FZK Cyclotron	3.13–10.0	13 533	[40]	3.5
Ohkubo (1984)	JAERI Linac	0.0008–0.93	310	[41]	2.5

already noticed in the R -matrix analysis of Ref. [44], where the transformation $E = 1.0012E_0 - 8617.7$ keV was suggested. This correction was also applied in the present work.

Since the Shouky *et al.* data exhibit large uncertainties from background subtraction below 1.6 MeV (which leads in some cases even to negative cross section values), only the data from Lane *et al.* [42] were used in this region. The elastic scattering data of Shouky *et al.* [43] have better resolution and cover a much wider energy range from 1.6 to 6.25 MeV, including resonances in the $^{13}\text{C}+\alpha$ channel up to 10 MeV excitation energy in ^{17}O . For both data sets, excellent agreement was consistently obtained in the R -matrix fits at all measured angles. This is demonstrated by the R -matrix fits of the data sets of Lane *et al.* and Shouky *et al.* in Figs. 11 and 12.

C. Inelastic double differential cross sections $^{16}\text{O}(n, n'\gamma)^{16}\text{O}$

In addition to the reaction channels mentioned above, double differential data for the inelastic cross section $^{16}\text{O}(n, n'\gamma)^{16}\text{O}$ from Nelson *et al.* [45] were also included in the R -matrix analysis (Table VI). These data probe mainly levels at higher excitation energies from 7.5 to 12 MeV in ^{17}O . The fit in Fig. 13 shows remarkably good agreement with the

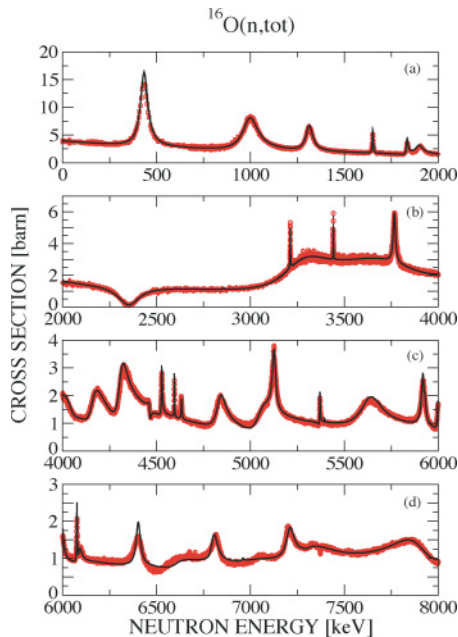


FIG. 10. (Color online) Total neutron cross section of ^{16}O (red symbols) compared to the R -matrix fit (black line). The α threshold in ^{17}O is at 2.35 MeV neutron energy. The resonance levels above that energy correspond to resonances in the $^{13}\text{C}+\alpha$ channel.

data, in particular in view of the enormous uncertainties in the resonance parameters at these high excitation energies.

D. Double differential cross section $^{13}\text{C}(\alpha, \alpha)^{13}\text{C}$

So far, only the measurements of Kerr *et al.* [32] and Barnes *et al.* [31] have been published for the elastic α scattering on ^{13}C . Unfortunately, neither data set is available in tabular form. Therefore, only data from the present work have been used to fit the elastic α scattering cross section. Table VII provides the information about the data sets used in this part of the analysis, and Figs. 14–16 show the resulting R -matrix fits.

Again, very good agreement is obtained for most scattering angles in the entire α energy range from 2.5 to 6.25 MeV with some minor deviations at higher energies. These deviations may come from false spin and parity assignments for high-energy levels in ^{17}O , where no spectroscopic information

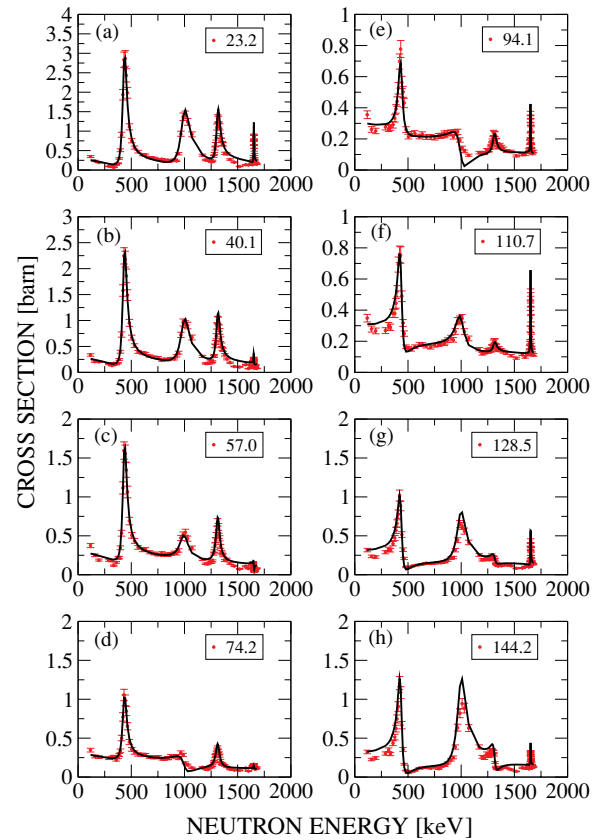


FIG. 11. (Color online) Comparison of the measured double differential elastic scattering cross section $^{16}\text{O}(n, n)$ from Lane *et al.* [42] (red symbols) and the R -matrix fit (black line).

TABLE V. Data sets for the double differential cross section of the $^{16}\text{O}(n, n)^{16}\text{O}$ reaction.

Authors	Facility	Energy range (MeV)	Angles (deg)	Data points	Ref.	χ^2
Lane <i>et al.</i> (1961)	Argonne, el.-stat. acc.	0.12–1.68	23.2, 40.1, 57.0, 74.2, 94.1, 110.7, 128.5, 144.2	680	[42]	17.1
Shouky <i>et al.</i> (1977)	FZK, Cyclotron	0.52–6.17	20, 30, 40, 55, 65, 80, 90, 120, 135, 150	8150	[43]	6.7

is available [35]. On the other hand, particularly good agreement is obtained with the low-energy scattering data, which correspond to the α energy range of interest for the present study.

E. Differential cross sections $^{13}\text{C}(\alpha, n)^{16}\text{O}$ and $^{16}\text{O}(n, \alpha)^{13}\text{C}$

The cross sections of $^{13}\text{C}(\alpha, n)$ and the inverse reaction $^{16}\text{O}(n, \alpha)^{13}\text{C}$ are especially important for the present analysis, since they are coupling both reaction channels. Tables VIII and IX give an overview of the data sets used. As discussed before, there are discrepancies in the normalization between various data sets for the $^{13}\text{C}(\alpha, n)^{16}\text{O}$ reaction. To produce consistent data, the sets of Bair and Haas [16] and Brune *et al.* [18,27] have been renormalized with factors of 0.804 and 1.20, respectively. The data set of Brune *et al.* contains multiple points near the two weak resonances at $E_\alpha = 656$ and 802 keV. The sharp resonance at $E_\alpha = 802$ keV revealed that the energy calibration of Drotleff *et al.* [10] was not in agreement with the time-of-flight data of the elastic neutron scattering channel by Shouky *et al.* [40] and of the total neutron cross section by Cierjacks *et al.* [40]. To remove this inconsistency the energies in the data set of Drotleff *et al.* [10] were corrected by a factor of 0.992.

The $^{16}\text{O}(n, \alpha)^{13}\text{C}$ cross section data by Seitz and Huber [46], Walton *et al.* [47], and Davis *et al.* [48] cover mainly an energy range well above the α threshold in ^{17}O . The fit provides an independent test of the reliability of higher energy resonance contributions to the $^{13}\text{C}(\alpha, n)^{16}\text{O}$ reaction channel.

Figure 17 shows the fits of the $^{16}\text{O}(n, \alpha)^{13}\text{C}$ and the $^{13}\text{C}(\alpha, n)^{16}\text{O}$ reaction cross sections. Overall excellent agreement was obtained between the experimental data and the R -matrix fit. Deviations appear only in the high-energy range of the $^{13}\text{C}(\alpha, n)^{16}\text{O}$ cross section since resonances above 10 MeV excitation energy in ^{17}O have not been taken into account.

The quality of the adopted data and the R -matrix fit was confirmed by a new measurement of the $^{13}\text{C}(\alpha, n)^{16}\text{O}$ cross section at higher energies. These data were published [26] after the rather extensive and time-consuming R -matrix analyses had been completed and therefore were not included in the original fitting effort. A comparison of the fit obtained in this work and the new data set is given in Fig. 17. It shows excellent agreement over the entire energy range. This not only underlines the quality of the present R -matrix analysis but also confirms the renormalization of the $^{13}\text{C}(\alpha, n)^{16}\text{O}$ data described above. The new data show a significantly better energy resolution than obtained by Bair and Haas and Sekharan *et al.* [37], and they also extend to higher excitation energies.

F. R -matrix resonance parameters

The fits demonstrate clearly that the cross sections at low excitation energies are characterized by single well-separated resonances. The interference patterns between the different resonant components can be clearly distinguished. That is important because this is the energy range of interest for the

TABLE VI. Data sets for the inelastic channels $^{16}\text{O}(n, n'\gamma)^{16}\text{O}$ and $^{16}\text{O}(n, \alpha\gamma)^{13}\text{C}$.

Authors	Facility	Energy range (MeV)	Angles (deg)	Data points	Ref.	χ^2
Nelson <i>et al.</i> (2001)	Los Alamos, LAMPF/WNR	5.03–19.98	90, 104, 110, 125, 131, 150, 159	1309	[45]	4.6

TABLE VII. Data sets for the double differential cross section of the $^{13}\text{C}(\alpha, \alpha)^{13}\text{C}$ reaction.

Authors	Facility	Energy range (MeV)	Angles (deg)	Data points	χ^2
This work	Notre Dame, 10 MV Tandem	2.9–6.2	44, 49, 54, 59, 64, 69, 74, 76, 79, 81, 84, 86, 89, 91, 94, 96, 99, 101, 106, 111, 116, 121, 126, 131, 141, 151, 161, 166	7700	13.4
This work	Notre Dame, 3.5 MV VdG	2.6–3.1	45, 65, 85, 105, 125, 145, 165	2064	4.0

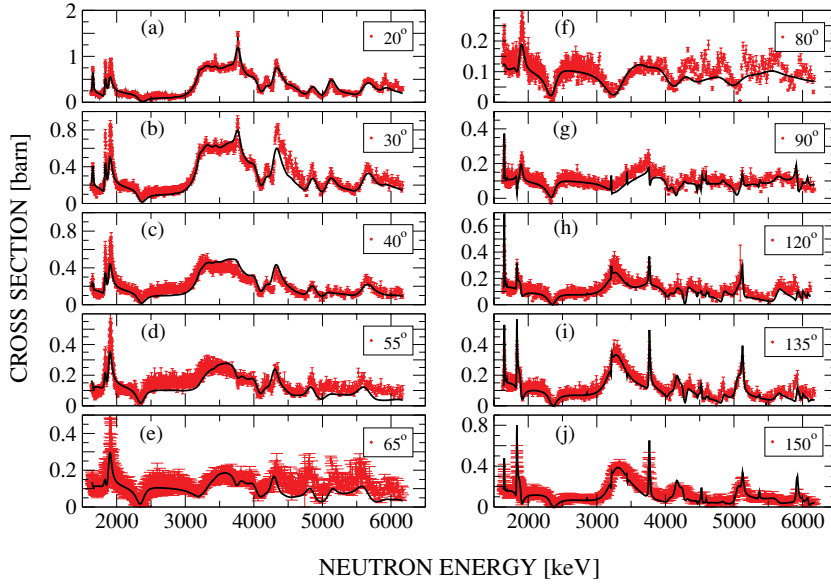


FIG. 12. (Color online) Comparison of the measured double differential elastic scattering cross section $^{16}\text{O}(n, n)$ from Shouky *et al.* [43] (red symbols) and the R -matrix fit (black line).

$^{13}\text{C}(\alpha, n)^{16}\text{O}$ reaction as an s -process neutron source. Also clearly reflected in the fits of the total neutron cross section of ^{16}O and the $^{16}\text{O}(n, n)$ elastic scattering channel is the opening of the α channel at 2.35 MeV, which is again critical for the overall quality of the resulting fit parameters of the contributing resonances. At higher excitation energies, many broad resonances start to overlap because of the increasing level density. In this range, the quality of the fits decreases, mainly because it was often not possible to clearly identify the individual resonances and to unambiguously determine their spin and parity values.

This is most obvious in the $^{13}\text{C}(\alpha, \alpha)^{13}\text{C}$ scattering data at energies above 4.5 MeV, which are also most sensitive to background terms. To mimic the influence of resonances outside the fitted region, background resonances for each spin group were postulated. In the case of the $^{13}\text{C}(\alpha, \alpha)^{13}\text{C}$ data, it was not possible to obtain a satisfying fit without including a broad $3/2^-$ background term.

The resonance parameters determined by simultaneous and self-consistent SAMMY R -matrix fits of all reaction channels are listed in Table X in comparison to the work of Sayer *et al.* [44], who focused their analysis on the description of the $^{16}\text{O}(n, x)$ cross sections. In general, there is good agreement, but more resonances could be included at excitation energies above 9900 keV based on the double differential $^{13}\text{C}(\alpha, \alpha)^{13}\text{C}$ cross section reported here. Because of the high level density in ^{17}O , many broad resonances are overlapping in this region; therefore it is very difficult to identify individual resonances and properly assign spin and parity values. Although the present resonance parameters describe the measured cross sections reasonably well, it cannot be excluded that different combinations of resonances with other spin and parity assignments give similar results. Regarding the $^{13}\text{C}(\alpha, n)^{16}\text{O}$ reaction, the first 12 resonances constitute negative-energy states, which were included for their effect on bound levels. To account for the influence of broad resonances at higher energies,

TABLE VIII. Data sets for the cross section of the $^{16}\text{O}(n, \alpha)^{13}\text{C}$ reaction.

Authors	Facility	Energy range (MeV)	Data points	Ref.	χ^2
Seitz <i>et al.</i> (1955)	Basel, 1 MV cascade acc.	3.6–4.2	25	[46]	1.5
Walton <i>et al.</i> (1957)	Wisconsin, el. stat. acc.	3.5–4.4	106	[47]	1.7
Davis <i>et al.</i> (1963)	Rice, VdG	5.0–8.8	160	[48]	3.2

TABLE IX. Data sets for the cross section of the $^{13}\text{C}(\alpha, n)^{16}\text{O}$ reaction.

Authors	Facility	Energy range (MeV)	Data points	Ref.	χ^2
Sekharan <i>et al.</i> (1966)	Bombay, VdG	1.95–5.57	155	[37]	2.8
Dauids (1968)	Caltech, el. stat. acc.	0.471–0.706	10	[15]	1.3
Bair and Haas (1973)	ORNL, 5.5 MV VdG	1.0–5.413	73	[16]	5.2
Brune <i>et al.</i> (1991)	Caltech,	0.656, 0.802		[18,27]	
and Kellogg <i>et al.</i> (1989)	0.7 MV Pelletron	0.448–1.0	13	[17]	0.2
Drotleff <i>et al.</i> (1993)	Stuttgart, 4 MV Dynamitron	0.35–1.4	55	[10]	1.1
This work	FZK, 3.7 MV VdG	0.414–0.899	14		0.3

TABLE X. Resonance parameters (in keV) used for the SAMMY fit.

Level	This work							Sayer <i>et al.</i> [44]			
	J^π	E_r	$E_x(^{17}\text{O})$	Γ_n	Γ_α	$\Gamma_{n'}$	$\Gamma_{n''}$	J^π	$E_x(^{17}\text{O})$	Γ_n	Γ_α
1	5/2+	-11022	-2069.6	455.6	1.3×10^{-6}	0.00	0.00	1/2+	-15447	9075	
2	1/2+	-7402.6	898.4	-5122	3.0×10^{-8}	0.00	0.00	1/2+	-8349.5	5410	
3	1/2-	-4391.1	3001.1	2.2×10^3	9.0×10^{-7}	0.00	0.00				
4	5/2-	-6529.9	1365.8	1.8×10^3	1.0×10^{-6}	0.00	0.00				
5	3/2-	-2364.2	4551.0	-43.4	9.9×10^{-7}	0.00	0.00	3/2-	4551.9	44.41	
6	3/2+	-1667.1	5084.0	-100.4	0.2	0.00	0.00	3/2+	5084.2	100.36	
7	9/2-	-1685.4	5070.1	6.8×10^{-7}	1.8×10^{-5}	0.00	0.00				
8	3/2-	-1286.2	5375.2	-42.1	4.3×10^{-7}	0.00	0.00	3/2-	5375.1	43.43	
9	7/2-	-865.8	5696.7	3.28	2.4×10^{-11}	0.00	0.00	7/2-	5696.7	4.1	
10	5/2-	-817.7	5733.5	0.09	4.1×10^{-9}	0.00	0.00	(5/2-)	5732.3	0.27	
11	3/2+	-641.2	5868.4	8.0	-4.1×10^{-4}	0.00	0.00	3/2+	5868.7	7.79	
12	1/2-	-569.7	5923.2	-48.1	5.5×10^{-9}	0.00	0.00	1/2-	5932.0	33.5	
13	1/2+	27.1	6379.5	158.1	1.7×10^{-54}	0.00	0.00	1/2+	6380.2	162.37	
14	5/2+	616.1	6829.8	0.32	1.1×10^{-6}	0.00	0.00	(5/2+)	6860.7	0.22	
15	7/2-	755.1	6936.2	8.7×10^{-3}	3.3×10^{-6}	0.00	0.00	(7/2-)	6971.9	0.16	
16	5/2-	1053.9	7164.6	1.88	4.3×10^{-3}	0.00	0.00	5/2-	7164.6	1.5	0.009
17	3/2+	1162.6	7247.7	340.1	0.14	0.00	0.00	3/2+	7239.1	339.63	0.17
18	5/2+	1332.9	7377.9	0.41	0.011	0.00	0.00	5/2+	7378.2	0.6	0.02
19	5/2-	1336.5	7380.7	1.77	2.9×10^{-3}	0.00	0.00	5/2-	7380.8	1.3	0.007
20	3/2-	1460.1	7475.2	678.3	0.027	0.00	0.00	3/2-	7446.9	660.21	0.026
21	7/2-	1735.8	7686.0	-14.5	0.011	0.00	0.00	7/2-	7686.9	18.53	0.026
22	1/2+	2103.2	7966.9	-94.0	2.64	0.00	0.00	1/2+	7963.3	105.58	5.23
23	1/2-	2032.4	7912.8	234.5	10.5	0.00	0.00	1/2-	7896.3	276.19	19.15
24	3/2+	2244.6	8075.1	87.3	7.1	0.00	0.00	3/2+	8075.4	92.38	9.8
25	1/2-	2401.5	8195.0	49.5	3.3×10^{-3}	0.00	0.00	1/2-	8199.3	43.52	-0.44
26	3/2-	2395.7	8190.6	-57.9	2.0	0.00	0.00	3/2-	8190.9	54.3	5.77
27	1/2+	2596.1	8343.8	8.6	1.5	0.00	0.00	1/2+	8345.7	16.89	3.72
28	5/2+	2672.3	8402.1	4.8	0.51	0.00	0.00	5/2+	8402.2	4.99	0.86
29	7/2+	2756.9	8466.8	-0.42	7.1	0.00	0.00	7/2+	8465.6	1.39	0.44
30	9/2+	2755.3	8465.6	-0.89	6.8×10^{-6}	0.00	0.00				
31	5/2-	2802.5	8501.6	2.23	3.12	0.00	0.00	5/2-	8499.8	3.2	3.88
32	3/2-	3037.0	8680.9	65.2	2.92	0.00	0.00	3/2-	8677.7	58.4	2.74
33	9/2-	3327.3	8902.9	-2.3×10^{-5}	-0.45	0.00	0.00				
34	3/2+	3338.8	8911.7	-101.8	25.3	0.00	0.00	3/2+	8909.1	94.5	-34.36
35	9/2-	3339.8	8912.4	-3.3×10^{-5}	-1.08	0.00	0.00				
36	7/2-	3407.6	8964.3	20.4	0.91	0.00	0.00	7/2-	8963.2	23.35	2.75
37	1/2-	3647.7	9147.9	0.23	7.33	0.00	0.00	(1/2-)	9139.3	0.5	4
38	9/2-	3739.7	9218.3	0.036	-0.044	0.00	0.00				
39	7/2-	3681.4	9173.7	0.038	3.26	0.00	0.00				
40	5/2+	3708.0	9194.0	2.29	0.24	0.00	0.00	5/2+	9194.1	2.78	1.25
41	3/2-	3972.2	9396.0	-200.5	0.30	0.00	0.00	3/2-	9387.5	191.17	0.42
42	5/2-	4096.7	9491.2	0.28	13.0	0.00	0.00	5/2-	9479.5	0.59	15.63
43	1/2+	4131.8	9518.0	-6.7×10^{-6}	127.8	0.00	0.00				
44	7/2+	4384.0	9710.9	17.5	1.36	0.00	0.00	7/2+	9710.9	20.5	4.19
45	7/2+	4394.4	9718.8	-2.45	4.81	0.00	0.00				
46	3/2+	4407.6	9728.9	1.92	70.0	0.00	0.00				
47	3/2-	4476.6	9781.7	16.5	3.4×10^{-6}	0.00	0.00	3/2-	9781.1	14.78	-0.21
48	9/2+	4577.7	9859.0	-2.44	0.47	0.00	0.00	9/2+	9859.1	3.13	2.51
49	1/2-	4586.6	9865.8	-29.0	1.72	0.00	0.00	(1/2-)	9869.7	16.04	1.92
50	7/2+	4711.3	9961.2	-1.81	-95.4	3.26	1.20	5/2+	9983.0	4.97	109.23
51	1/2+	4817.1	10042	-7.2×10^{-5}	-48.9	0.019	4.1×10^{-4}	7/2+	10100	3.4	181.48
52	5/2-	4978.0	10165	24.5	4.92	71.8	2.3×10^{-6}	(7/2-)	10164	26.54	29.38
53	5/2+	5029.0	10204	-9.7×10^{-6}	303.3	0.027	3.4×10^{-3}				
54	1/2-	4981.9	10168	26.0	245.0	4.1×10^{-4}	0.12				
55	3/2+	5226.4	10355	55.9	86.5	7.1×10^{-7}	3.4×10^{-4}	3/2+	10331.2	90.64	87.94
56	3/2-	5256.5	10378	9.8×10^{-3}	1.65	1.14	1.3×10^{-6}				

TABLE X. (*Continued.*)

Level	This work							Sayer <i>et al.</i> [44]			
	J^π	E_r	$E_x(^{17}\text{O})$	Γ_n	Γ_α	$\Gamma_{n'}$	$\Gamma_{n''}$	J^π	$E_x(^{17}\text{O})$	Γ_n	Γ_α
57	5/2−	5431.8	10512	-9.1×10^{-5}	−54.2	24.8	2.36	5/2−	10420.3	1.86	19.06
58	7/2+	5460.7	10534	−3.05	74.8	22.0	0.10	5/2+	10526.9	10.57	232.54
59	5/2−	5485.5	10553	−18.6	−4.39	18.6	7.4×10^{-6}	(7/2−)	10554.2	18.94	28.36
60	9/2+	5664.8	10690	0.12	−6.94	4.8×10^{-5}	1.63				
61	3/2−	5784.8	10782	150.0	−82.1	0.079	192.4				
62	1/2+	5848.6	10831	1.4×10^{-5}	107.0	5.74	43.5	7/2−	10886.8	129.69	223.85
63	5/2−	5970.7	10924	−32.3	10.6	1.35	20.9	(5/2+)	10914.7	7.86	19.7
64	1/2−	6249.4	11137	−154.0	−618.1	0.89	2.6×10^{-3}	1/2−	11004.9	26.16	5.39
65	9/2+	6171.9	11078	23.3	71.9	650.6	0.06	1/2−	11079.3	1.89	
66	1/2−	5855.2	10836	29.4	890.4	126.2	10.9				
67	5/2+	6110.9	11031	−2.05	33.6	4.3×10^{-4}	13.8				
68	9/2−	6318.9	11190	56.8	−0.014	7.6×10^{-4}	1133				
69	7/2+	6768.6	11534	83.9	-7.5×10^{-7}	144.4	67.4				
70	7/2+	7551.9	12133	384.1	−9.68	275.5	99270				
71	5/2+	8937.5	13193	191.3	1199	74146	3477				
72	3/2+	7806.6	12328	461.5	1.24	1.8	39.5				
73	7/2−	11770	15359	−7980	258.7	809.7	227.7				
74	9/2−	11873	15437	158.6	−153.9	0.31	7.93				
75	1/2+	14190	17209	868.8	1285	23911	823.1				
76	1/2−	9582.5	13686	8166	0.0	0.0	2056	1/2−	22051	25755	
77	3/2−	10834	14643	18070	605.4	68.7	427.6	3/2−	14620	15115	
78	3/2+	12204	15691	19.3	24506	2.47	60980	3/2+	20354	772.36	
79	5/2+	17002	19359	−65.6	0.12	34.8	12780				
80	5/2−	12860	16192	−2.1	13748	0.0	3.31				
81	7/2−	12277	15747	97.8	34437	55995	0.00				
82	7/2+	13187	16442	−836.7	7888	4160	6.45				
83	9/2+	19018	20900	−24220	0.0	104.2	2714				
84	9/2−	16621	19068	43242	7.37	2619	6.05				

background resonances were also included (last ten resonances in Table X).

V. S-FACTOR EXTRAPOLATION OF THE $^{13}\text{C}(\alpha, n)^{17}\text{O}$ REACTION DATA

The R -matrix fits can be seen in Figs. 10–17, and the χ^2 values of the individual data sets are given in Tables IV–IX. As discussed before, excellent agreement between the fits and the data points was obtained for all reaction channels.

Using the best fit parameters listed in Table X, the astrophysical S factor for the $^{13}\text{C}(\alpha, n)^{16}\text{O}$ reaction has been extrapolated into the low-energy range of stellar helium burning. As shown in Fig. 18, the S factor clearly increases toward lower energies, according to constructive interference with the $1/2^+$ resonance at 6.356 MeV excitation energy, 3 keV below the reaction threshold. This increase in the S factor is substantially stronger than suggested by Kubono *et al.* [8], who had proposed a weak α strength for this level on the basis of a distorted-wave Born approximation (DWBA) $^{13}\text{C}(^6\text{Li}, d)^{17}\text{O}$ α transfer analysis. Our results suggest a considerably stronger contribution of this level, which supports the conclusion of Keeley *et al.* [9] obtained in a reanalysis of these $^{13}\text{C}(^6\text{Li}, d)^{17}\text{O}$ α transfer data.

The uncertainty range of the S -factor curve indicated by the dashed lines in Fig. 18 is dominated by the uncertainty of the resonance parameters of the broad $3/2^+$ state at 7.248 MeV excitation energy as well as by the parameters of the threshold state at 6.379 MeV ($1/2^+$) and of the subthreshold states at 5.923 MeV ($1/2^-$) and 5.868 MeV ($3/2^+$), and by the associated interference pattern. To estimate the uncertainty of the low-energy S factor, the α partial widths Γ_α of the $J^\pi = 1/2^+$ threshold level as well as of the two subthreshold resonances at $E_\alpha = -567$ and -641 keV were varied by certain factors around the parameters of the best fit. Keeping the chosen α partial widths constant, all other parameters were fitted freely to the data. The resulting χ^2 was recorded as function of the obtained S factor. According to Ref. [49], the uncertainty of the parameter is given by the boundaries, when the change for χ^2 is equal to unity. The corresponding results for the resonances at 6.379 MeV ($1/2^+$) and 5.868 MeV ($3/2^+$) are plotted in Fig. 19, which demonstrates the relative impact of the different levels on the S -factor extrapolation. The $J^\pi = 1/2^-$ resonance at $E_\alpha = -567$ keV has only limited influence and is not shown. Although the α partial width was varied by a factor of 1000, the resulting χ^2 value and, more importantly, the overall S factor did not vary much. This demonstrates that the α partial width is well constrained by the data and the level does not

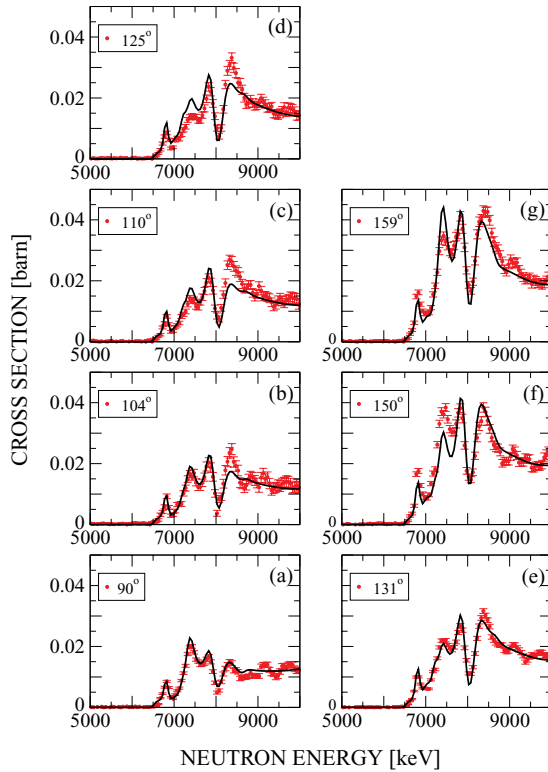


FIG. 13. (Color online) R -matrix fit (black line) of the inelastic channels $^{16}\text{O}(n, n'\gamma)^{16}\text{O}$ and $^{16}\text{O}(n, \alpha\gamma)^{13}\text{C}$ from Nelson *et al.* [45] (red symbols).

contribute significantly to the uncertainty of the low-energy S factor. For the $J^\pi = 3/2^+$ resonance at $E_\alpha = -641$ keV the α width was varied by factors from 0.25 to 3. This variation results in a large increase in χ^2 , which is caused by the strong interference with the broad $J^\pi = 3/2^+$ resonance at $E_\alpha = 800$ keV. Therefore, the parameters of this resonance are

well constrained by the data, and the uncertainty introduced in the S -factor extrapolation is very small.

Finally, the influence of the $J^\pi = 1/2^+$ close to the reaction threshold needs to be considered. A variation of the resonance parameter Γ_α by factors between 0.17 and 2.5 causes only small changes in the χ^2 value but has significant consequences for the S factor. Hence, the uncertainty in this parameter is responsible for most of the uncertainty in our S -factor extrapolation. Unfortunately, the indirect studies discussed before have not succeeded in reducing this uncertainty by obtaining the reduced α width or ANC for this level. Since the results of these experiments differ substantially, these values may depend significantly on the choice of reaction or reaction model parameters.

The comparison of the S -factor curve obtained in the present analysis with previous predictions and the recent ANC measurements is shown in Fig. 20. The S -factor prediction based on the generalized cluster model (GCM) normalized to experimental results by Descouvemont [6] shows excellent agreement within the given uncertainty range with the here-obtained S -factor curve. On the other hand, the R -matrix extrapolation by Hale [14] reaches substantially larger values for the low-energy S factor than predicted in the present work. While no details on the R -matrix levels have been provided by Hale, the results suggest that the fit clearly overestimates the influence of the subthreshold level at 6.379 MeV ($1/2^+$). His results indicate a reduced α -width amplitude reaching nearly the single-particle limiting value. While his results seem consistent with the experimental data available for his R -matrix fit, the more recent experimental ANC studies clearly indicate that the reduced width amplitude for at least the $1/2^+$ subthreshold level is significantly smaller [7,34].

R -matrix fits were also provided on the basis of the two ANC measurements using the $^{13}\text{C}(^6\text{Li}, d)^{17}\text{O}$ α transfer reaction at sub-Coulomb energies of 8 keV [7] and the $^{13}\text{C}(^7\text{Li}, t)^{17}\text{O}$ transfer reaction at high energies of 28 and 32 MeV [34], respectively. The ANC analysis leads to very different ANC

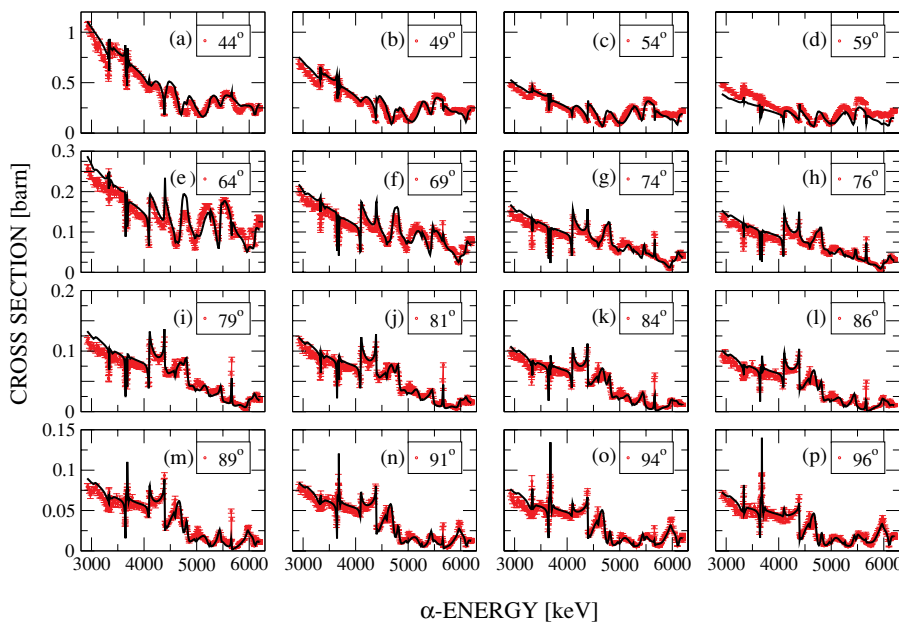


FIG. 14. (Color online) Comparison of the measured double differential elastic scattering cross section $^{13}\text{C}(\alpha, \alpha)^{13}\text{C}$ of this work (symbols) and the R -matrix fit (black line). Shown are the detectors from 44° to 96° .

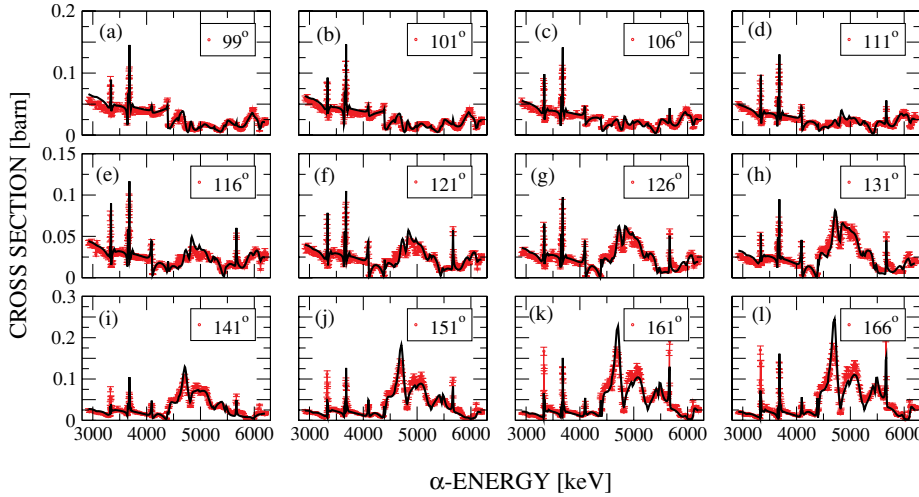


FIG. 15. (Color online) Same as Fig. 14, but for the detectors from 99° to 166°.

values for the threshold state, which directly translates into a substantially different S -factor prediction in the R -matrix analysis. The choice of energy may have affected the result, since the ANC approach requires a peripheral reaction mechanism, which is better warranted at sub-Coulomb energies. The direct comparison of the R -matrix fits provided on the basis of the respective ANC analyses is shown in Fig. 20. In both cases, the R -matrix analysis is restricted to $^{13}\text{C}(\alpha, n)^{17}\text{O}$ compound levels near the α threshold up to ≈ 8 MeV excitation energy. Johnson *et al.* [7] restricted the fit to the variation of the α partial widths of the contributing resonances, while Pellegriti *et al.* [34] also varied the neutron partial widths of the states. Their results indicate, for example, a much broader total width for the $3/2^+$ resonance at 7.248 MeV than that adopted by Johnson *et al.* [7,35], in good agreement with the resonance parameters obtained in the present study.

The R -matrix S -factor extrapolation by Johnson *et al.* [7] shows a much reduced increase compared to the here-presented fits because of the low ANC obtained for the $1/2^+$ resonance state at 6.379 MeV excitation energy. The S -factor curve matches the lower limit of our R -matrix predictions.

On the other hand, the results by Pellegriti *et al.* [34] yield an ANC value, which is about a factor of 5 higher, causing a much steeper increase of the S -factor curve. This is further enhanced by the broader total widths predicted by the R -matrix simulation for this level and for the $3/2^+$ resonance state at 7.248 MeV. The prediction for the S -factor matches our present R -matrix simulations.

VI. STELLAR REACTION RATE FOR $^{13}\text{C}(\alpha, n)^{16}\text{O}$

Tabulated values of the calculated $^{13}\text{C}(\alpha, n)^{16}\text{O}$ reaction rate can be found in Table XI. In Fig. 21, the rate is compared with previous compilations by Caughlan and Fowler [11], Denker and Hammer [12], and with the NACRE compilation [13]. Table XII compares the reaction rates at the astrophysically relevant temperature of 0.1×10^9 K.

In general, these rates agree within a factor of 2, except for the larger discrepancy of the Caughlan and Fowler rate at low temperatures. This difference can be explained, since the low-energy contributions of the subthreshold resonances have

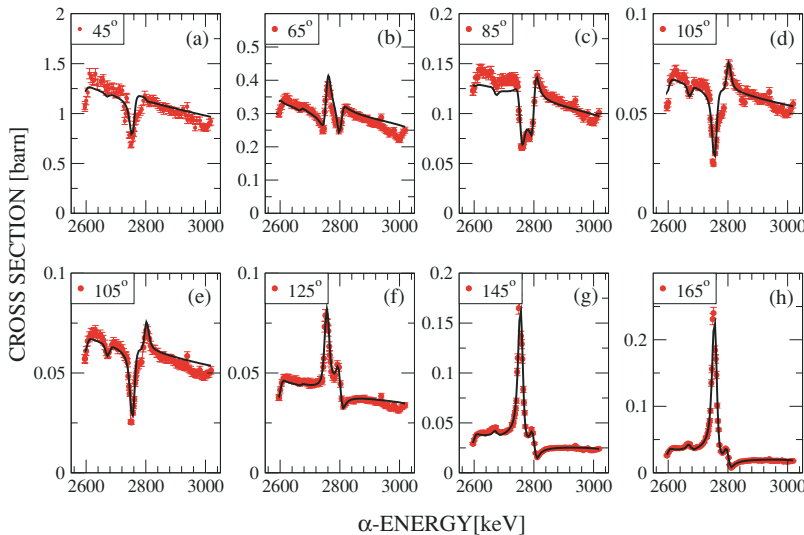


FIG. 16. (Color online) Same as Fig. 14, but for the detectors from 45° to 165°.

TABLE XI. Reaction rate of the $^{13}\text{C}(\alpha, n)^{16}\text{O}$ reaction.

Temperature (10^9 K)	Reaction rate ($\text{cm}^3/\text{mole s}$)	Temperature (10^9 K)	Reaction rate ($\text{cm}^3/\text{mole s}$)
0.04	2.72×10^{-24}	0.29	1.80×10^{-5}
0.05	1.73×10^{-21}	0.30	3.09×10^{-5}
0.06	2.34×10^{-19}	0.32	8.57×10^{-5}
0.07	1.17×10^{-17}	0.34	2.21×10^{-4}
0.08	2.94×10^{-16}	0.36	5.35×10^{-4}
0.09	4.46×10^{-15}	0.38	1.23×10^{-3}
0.10	4.64×10^{-14}	0.40	2.67×10^{-3}
0.11	3.60×10^{-13}	0.42	5.55×10^{-3}
0.12	2.21×10^{-12}	0.44	1.11×10^{-2}
0.13	1.12×10^{-11}	0.46	2.12×10^{-2}
0.14	4.84×10^{-11}	0.48	3.91×10^{-2}
0.15	1.84×10^{-10}	0.50	6.98×10^{-2}
0.16	6.23×10^{-10}	0.52	0.12
0.17	1.92×10^{-9}	0.54	0.20
0.18	5.45×10^{-9}	0.56	0.33
0.19	1.44×10^{-8}	0.58	0.52
0.20	3.56×10^{-8}	0.60	0.81
0.21	8.35×10^{-8}	0.65	2.18
0.22	1.86×10^{-7}	0.70	5.20
0.23	3.97×10^{-7}	0.75	11.2
0.24	8.12×10^{-7}	0.80	22.2
0.25	1.60×10^{-6}	0.85	41.0
0.26	3.06×10^{-6}	0.90	71.0
0.27	5.67×10^{-6}	0.95	117
0.28	1.02×10^{-5}	1.00	184

not been taken into account in their work. The NACRE result is based on a Breit-Wigner fit of the tail of the subthreshold resonance ($J^\pi = 1/2^+$) by Drotleff *et al.* [10], which suggests a stronger contribution of this level than obtained in the present *R*-matrix analysis of the same data. This resulted in a reaction rate prediction that is a factor of 2 higher than suggested in our analysis.

Very good agreement was found with the rate reported by Denker and Hammer [12], which is currently used in most stellar model codes. The fact that this rate was confirmed to better than 20% over the entire energy region resolves previous discrepancies and consolidates the strength of the $^{13}\text{C}(\alpha, n)^{16}\text{O}$ neutron source in stellar *s*-process models.

TABLE XII. Comparison of stellar rates (in units of $10^{-14} \text{ cm}^3/\text{mole s}$) for the $^{13}\text{C}(\alpha, n)$ reaction at $T = 0.1 \times 10^9$ K.

Authors	Reaction rate	Ref.
Caughlan and Fowler (1988)	2.58	[11]
Denker and Hammer (1995)	4.32	[12]
NACRE (1999)	$7.24^{+1.25}_{-4.98}$	[13]
This work	4.6 ± 1.0	

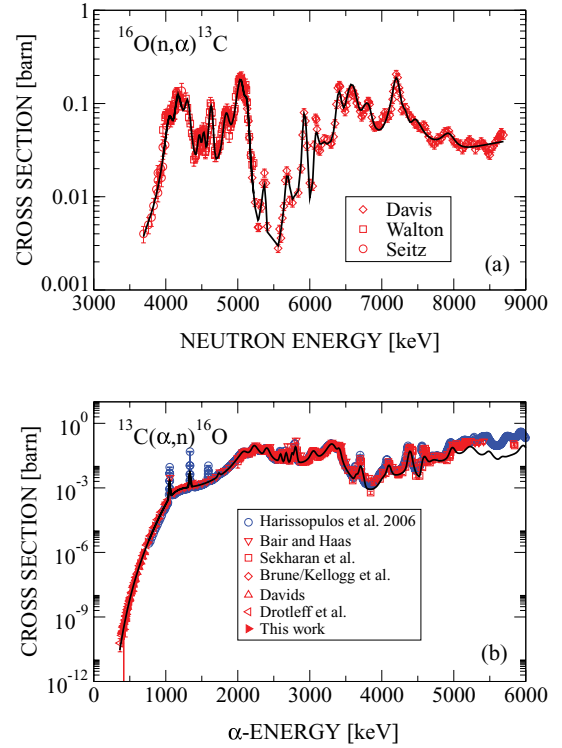


FIG. 17. (Color online) Fit of the $^{13}\text{C}(\alpha, n)^{16}\text{O}$ cross section (bottom) and the inverse reaction channel $^{16}\text{O}(n, \alpha)^{16}\text{O}$ (top). The individual data sets are marked with red symbols and the *R*-matrix fit with a black line.

VII. SUMMARY

The aim of this work was to determine the stellar rate for the $^{13}\text{C}(\alpha, n)^{16}\text{O}$ reaction at the astrophysically relevant thermal energy of $kT = 8$ keV. According to current stellar models, $^{13}\text{C}(\alpha, n)^{16}\text{O}$ is considered to be the main neutron source for the *s* process, operating at a temperature of

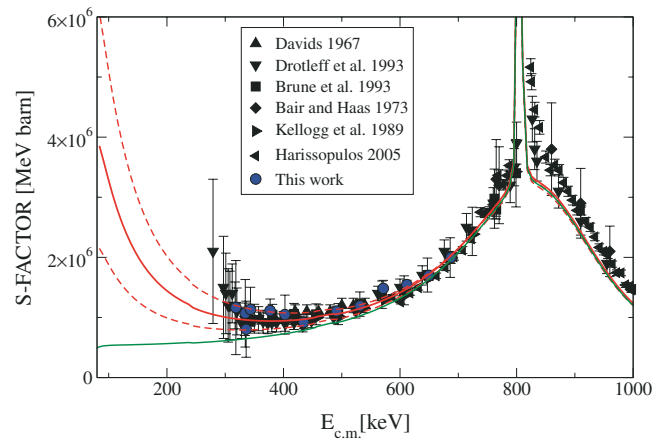


FIG. 18. (Color online) Extrapolation of the astrophysical *S* factor for the $^{13}\text{C}(\alpha, n)^{16}\text{O}$ reaction to the energy range of stellar helium burning by means of the *R*-matrix fit [upper solid (red) line]. The present error bars are indicated by dashed lines. The lower solid (green) line corresponds to an extrapolation in which the $J^\pi = 1/2^+$ resonance slightly below the reaction threshold was omitted.

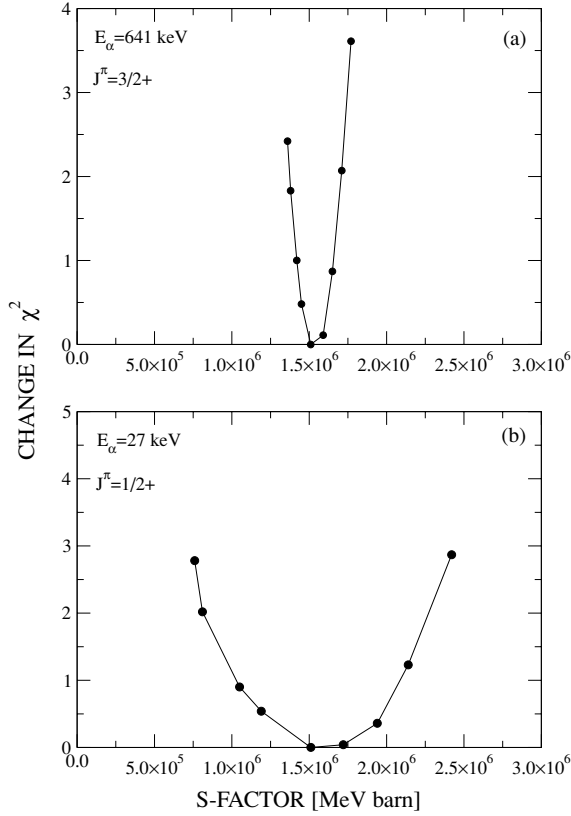


FIG. 19. Effect of the variation of the α parameters of the important threshold and subthreshold states on the quality of the R -matrix fits. The plots show the variation of χ^2 when the width of the α channel was changed around the best value.

90×10^6 K ($kT = 8$ keV) under radiative conditions between He shell flashes in thermally pulsing low mass AGB stars [1]. A thermal energy of $kT = 8$ keV is equivalent to a Gamow window around 190 keV for α particles. Since this energy is far below the Coulomb barrier, the reaction cross section is extremely small and cannot be measured directly. Therefore

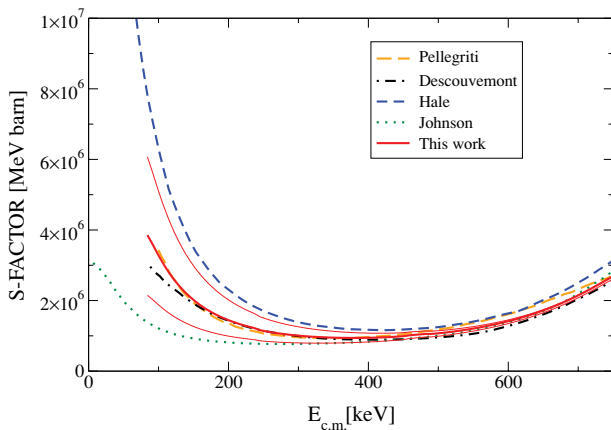


FIG. 20. (Color online) Comparison of the S -factor curve obtained in the present analysis with previous predictions and the recent ANC measurements. The thin red lines indicate the error band of this work.

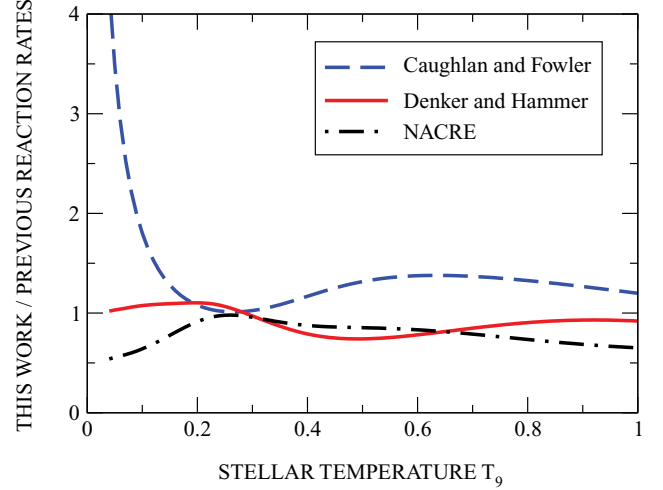


FIG. 21. (Color online) Present reaction rate for $^{13}\text{C}(\alpha, n)^{16}\text{O}$ divided by the results of the previous compilations by Caughlan and Fowler [11], Denker and Hammer [12], and the NACRE Collaboration [13].

one has to rely on the extrapolation of the values measured at higher energies. In this work, an extensive R -matrix analysis was carried out, which for the first time, accounts for all possible reaction channels. To increase the reliability of the extrapolation, the existing data have been complemented by two experiments.

First, the absolute cross section of the $^{13}\text{C}(\alpha, n)$ reaction was measured in the energy range $E_{\text{c.m.}} = 320\text{--}700$ keV with an accuracy of $\pm 5\%$ in order to resolve the discrepancies in the normalization of previous data sets. Second, the double differential scattering cross section $^{13}\text{C}(\alpha, \alpha)^{13}\text{C}$ was measured in the energy range $E_{\text{lab}} = 2.5\text{--}6.2$ MeV for 28 angles. These data were used to constrain possible contributions from background resonances and, therefore, contributed significantly to improving the accuracy of the R -matrix extrapolation of the S factor into the Gamow window. In addition, the spin and parity assignments have been improved for many resonances.

Our extrapolation yields a reaction rate of $(4.6 \pm 1.0) \times 10^{-14}$ cm³/mole s at $kT = 8$ keV ($T = 0.1 \times 10^9$ K) with a significantly improved accuracy compared to previous results. The present result agrees with the rate of Denker and Hammer [12] to better than 20% over the entire energy region. This represents an important point, since it resolves previous discrepancies and consolidates the strength of the $^{13}\text{C}(\alpha, n)^{16}\text{O}$ neutron source in stellar s -process models.

Any further improvement of the stellar rate requires an extension of the experimental data toward lower energies. Since the present technical possibilities appear to be exhausted, a reduction of the remaining uncertainty can probably only be achieved in an underground laboratory, where the cosmic-ray-induced γ background can be avoided.

ACKNOWLEDGMENTS

We thank especially Nancy Larson for all the support concerning R -matrix issues. We are thankful to D. Roller, E.-P. Knaetsch, and W. Seith for their support during the

$^{13}\text{C}(\alpha, n)$ measurements. This work was supported by the National Science Foundation under Grant No. PHY01-40324

and the Joint Institute for Nuclear Astrophysics, NSF-PFC, under Grant No. PHY02-16783.

-
- [1] R. Gallino *et al.*, *Astrophys. J.* **497**, 388 (1998).
 - [2] F. Herwig, T. Blöcker, D. Schönberner, and M. El Eid, *Astron. Astrophys.* **324**, L81 (1997).
 - [3] F. Herwig and N. Langer, *Mem. Soc. Astron. It.* **72**, 277 (2001).
 - [4] F. Herwig, N. Langer, and M. Lugaro, *Astrophys. J.* **593**, 1056 (2003).
 - [5] L. Siess, S. Goriely, and N. Langer, *Astron. Astrophys.* **415**, 1089 (2004).
 - [6] P. Descouvemont, *Phys. Rev. C* **36**, 2206 (1987).
 - [7] E. D. Johnson *et al.*, *Phys. Rev. Lett.* **97**, 192701 (2006).
 - [8] S. Kubono *et al.*, *Phys. Rev. Lett.* **90**, 062501 (2003).
 - [9] P. Keeley, K. Kemper, and D. T. Khoa, *Nucl. Phys. A* **726**, 159 (2003).
 - [10] H. Drotleff *et al.*, *Astrophys. J.* **414**, 735 (1993).
 - [11] G. Caughlan and W. Fowler, *At. Data Nucl. Data Tables* **40**, 291 (1988).
 - [12] A. Denker and J. Hammer, in *Nuclei in the Cosmos '94*, edited by M. Busso, R. Gallino, and C. Raiteri (AIP, New York, 1995), p. 255.
 - [13] C. Angulo *et al.*, *Nucl. Phys.* **A656**, 3 (1999).
 - [14] G. Hale, *Nucl. Phys.* **A621**, 177c (1997).
 - [15] C. Davids, *Nucl. Phys.* **A110**, 619 (1968).
 - [16] J. Bair and F. Haas, *Phys. Rev. C* **7**, 1356 (1973).
 - [17] S. Kellogg, R. Vogelaar, and R. Kavanagh, *Bull. Am. Phys. Soc.* **34**, 1192 (1989).
 - [18] C. R. Brune, I. Licot, and R. W. Kavanagh, *Phys. Rev. C* **48**, 3119 (1993).
 - [19] M. Heil, Rep. FZKA-6783, 2002 (unpublished).
 - [20] K. Wisshak *et al.*, *Nucl. Instrum. Methods Phys. Res. A* **292**, 595 (1990).
 - [21] K. Wisshak, K. Guber, F. Käppeler, and F. Voss, *Nucl. Instrum. Methods Phys. Res. A* **299**, 60 (1990).
 - [22] J. Apostolakis, CERN Tech. Rep., GEANT library, <http://wwwinfo.cern.ch/asd/geant/>.
 - [23] J. Stoner Jr., J. Borgardt, M. Ashbaugh, and L. McIntyre Jr., *Nucl. Instrum. Methods Phys. Res. A* **480**, 133 (2002).
 - [24] F. Ajzenberg-Selove, *Nucl. Phys.* **A506**, 1 (1990).
 - [25] J. Ziegler, *Handbook of Stopping Cross-Sections for Energetic Ions in All Elements* (Pergamon, New York, 1980), Vol. 5.
 - [26] S. Harissopulos, H. W. Becker, J. W. Hammer, A. Lagoyannis, C. Rolfs, and F. Strieder, *Phys. Rev. C* **72**, 062801(R) (2005).
 - [27] C. R. Brune and R. W. Kavanagh, *Phys. Rev. C* **45**, 1382 (1992).
 - [28] Y. Baudinet-Robinet, *Nucl. Instrum. Methods* **190**, 197 (1981).
 - [29] F. Ajzenberg-Selove, *Nucl. Phys.* **A413**, 1 (1984).
 - [30] F. Ajzenberg-Selove, *Nucl. Phys.* **A475**, 1 (1987).
 - [31] B. Barnes, T. Belote, and J. Risser, *Phys. Rev.* **140**, B616 (1965).
 - [32] G. Kerr, J. Morris, and J. Risser, *Nucl. Phys.* **A110**, 637 (1968).
 - [33] P. Descouvemont and T. Rauscher, *Nucl. Phys.* **A777**, 137 (2006).
 - [34] M. G. Pellegriti *et al.*, *Phys. Rev. C* **77**, 042801 (2008).
 - [35] D. Tilley and H. Weller, *Nucl. Phys.* **A564**, 1 (1993).
 - [36] N. Larson, Rep. ORNL/TM-9179/R5, 2000 (unpublished).
 - [37] K. Sekharan, A. Divatia, and M. Metha, *Phys. Rev.* **156**, 1187 (1967).
 - [38] S. Cierjacks *et al.*, Rep. KFK-1000, 1968 (unpublished).
 - [39] J. L. Fowler, C. H. Johnson, and R. M. Feezel, *Phys. Rev. C* **8**, 545 (1973).
 - [40] S. Cierjacks *et al.*, *Nucl. Instrum. Methods* **169**, 185 (1980).
 - [41] M. Ohkubo, private communication to NNDC (unpublished).
 - [42] R. O. Lane, A. S. Langsdorf, J. E. Monahan, and A. J. Elwyn, *Ann. Phys.* **12**, 135 (1961).
 - [43] I. Shouky, Rep. KFK-2503, 1977 (unpublished).
 - [44] R. Sayer *et al.*, Rep. ORNL/TM-2000/212, 2000 (unpublished).
 - [45] R. Nelson, M. Chadwick, A. Michaudon, and P. Young, *Nucl. Sci. Eng.* **138**, 105 (2001).
 - [46] J. Seitz and P. Huber, *Helv. Phys. Acta* **28**, 227 (1955).
 - [47] R. B. Walton, J. D. Clement, and F. Boreli, *Phys. Rev.* **107**, 1065 (1957).
 - [48] E. Davis, T. Bonner, J. Worley, and R. Bass, *Nucl. Phys.* **48**, 169 (1963).
 - [49] *Data Reduction and Error Analysis for the Physical Sciences*, edited by P. Bevington and D. Robinson (McGraw-Hill, New York, 1994).